Charge singlets and orbital-selective charge density wave transitions

Yuxi Zhang,[1] Chunhan Feng,[1] Rubem Mondaini,[2] G. G. Batrouni,[3,4,5,2] and Richard T. Scalettar[1]
[1]*Department of Physics, University of California, Davis, California 95616, USA*
[2]*Beijing Computational Science Research Center, Beijing 100084, China*
[3]*Université Côte d'Azur, CNRS, Institut de Physique de Nice (INPHYNI), 06000 Nice, France*
[4]*Centre for Quantum Technologies, National University of Singapore, 2 Science Drive 3, 117542 Singapore*
[5]*Department of Physics, National University of Singapore, 2 Science Drive 3, 117542 Singapore*

(Received 5 October 2021; revised 22 August 2022; accepted 23 August 2022; published 12 September 2022; corrected 24 May 2023)

The possibility of "orbitally selective Mott transitions" within a multiband Hubbard model, in which one orbital with large on-site *electron-electron repulsion* U_1 is insulating and another orbital, to which it is hybridized, with small U_{-1}, is metallic, is a problem of long-standing debate and investigation. In this paper we study an analogous phenomenon, the coexistence of metallic and insulating bands in a system of orbitals with different *electron-phonon coupling*. To this end, we examine two variants of the bilayer Holstein model: a uniform bilayer and a "Holstein-metal interface" where the electron-phonon coupling, λ, is zero in the "metallic" layer. In the uniform bilayer Holstein model, charge density wave (CDW) order dominates at small interlayer hybridization t_3, but decreases and eventually vanishes as t_3 grows, providing a charge analog of singlet (spin liquid) physics. In the interface case, we show that CDW order penetrates into the metal layer and forms long-range CDW order at an intermediate ratio of inter- to intralayer hopping strengths, $1.4 \lesssim t_3/t \lesssim 3.4$. This is consistent with the occurrence of an "orbitally selective CDW" regime at weak t_3 in which the layer with $\lambda_1 \neq 0$ exhibits long-range charge order, but the "metallic layer" with $\lambda_{-1} = 0$, to which it is hybridized, does not.

DOI: 10.1103/PhysRevB.106.115120

I. INTRODUCTION

Over the last several decades, much attention has been focused in the condensed matter community on layered materials. One prominent example is that of the cuprate superconductors [1–5]. Bilayer graphene [6–11] is another, more recent, realization. From a theoretical perspective, bilayer materials offer an opportunity to explore the competition between the formation of long-range order at weak interlayer coupling and collections of independent local degrees of freedom in the limit of strong interlayer coupling. Computational studies have lent considerable insight into these phenomena, including quantitative values for the quantum critical points [12–16] separating antiferromagnetic and singlet phases at zero temperature.

This competition is central to that which occurs in multiorbital systems, notably the interplay of Ruderman-Kittel-Kasuya-Yosida order and singlet formation in the Kondo lattice and periodic Anderson models [17–19]. This close analogy originates in the observation that, in calculations on a model Hamiltonian, there is no difference between multilayer and multiorbital descriptions, apart from the interpretation of the additional label of the fermionic species. For this reason we will use the two terminologies interchangeably here. In multiorbital language, one of the key conceptual interests is the possibility that the distinct values of the ratio of interaction strength to kinetic energy in the different bands might result in *separate* insulator transitions, i.e., the possibility of an "orbital-selective" Mott transition [20–31].

Here we study analogous questions concerning bilayer (biorbital) systems in which the fermions interact with phonon degrees of freedom rather than via direct electron-electron correlations. A precise mathematical description of the mapping between the two situations is discussed. Quantum Monte Carlo (QMC) simulations have already been applied to the analysis of charge-density wave (CDW) and superconducting transitions in the single-band Holstein model [32]. However, thus far, work has focused mostly on two-dimensional or three-dimensional models with a single kinetic energy scale [33–46].

Using QMC simulations of the two-band Holstein model at half-filling, we will address the following questions concerning the effects of interband hybridization t_3: (i) Is there a transition in which CDW order is destroyed as t_3 is increased? What is the value of the critical coupling associated with the quantum critical point (QCP) in the ground state and the critical temperature for the thermal transitions at finite T? (ii) In a situation where the electron-phonon energy scales in the two bands are very different, can CDW order in one band coexist with metallic behavior in the other? These issues are in direct analogy with those addressed in multiband Hubbard Hamiltonians; we will discuss similarities and differences between the resulting phenomena.

The paper is organized as follows: Section II starts by describing the model Hamiltonian, with Sec. III introducing the numerical algorithm employed. The main results of both the bilayer Holstein model and the Holstein-metal interface are given in Secs. IV and V, respectively. A contrast

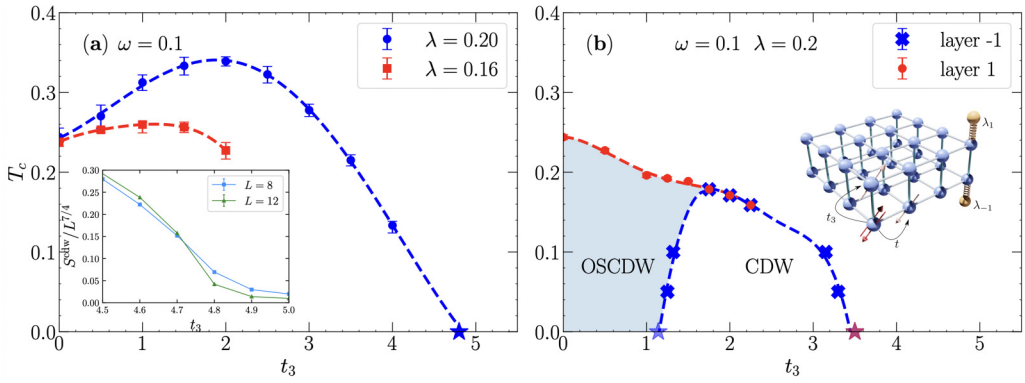

FIG. 1. (a) Phase diagram of the Holstein bilayer giving the CDW transition temperature T_c as a function of interlayer hopping t_3. Two values of electron-phonon coupling, $\lambda = 0.2$ and $\lambda = 0.16$, are shown. Data points are obtained by finite size scaling (FSS) analysis as shown in Fig. 3. Dashed lines are guides to the eye. Inset shows crossing plot of $S^{\rm CDW}/L^{7/4}$ versus t_3 at $\lambda = 0.2$ and low temperature $\beta = 20$ and determines the quantum critical value for the CDW charge singlet transition. (b) Analog of (a), but for the Holstein-metal interface. The four data points (blue crosses) at $T = 0.1$ and $T = 0.05$ are obtained by analysis of the scaled structure factor, Fig. 6. Inset shows a sketch of a bilayer with relevant terms in Eq. (1) marked. QCPs are marked by stars on the t_3 axes in panels (a) and (b). The phonon frequency $\omega = 0.1$ for all data.

between the two models is drawn in Sec. VI, by analyzing local quantities and gaps to excitations. Section VII summarizes our results.

II. LAYERED HOLSTEIN HAMILTONIAN

We focus on the bilayer Holstein model

$$\hat{\mathcal{H}} = -\sum_{\langle ij\rangle,l,\sigma}(t_l\,\hat{c}^\dagger_{il\sigma}\hat{c}_{jl\sigma} + \text{H.c.}) - \sum_{i,l,\sigma}\mu_l\hat{n}_{il\sigma} + \frac{1}{2M}\sum_{il}\hat{P}^2_{il} + \frac{1}{2}\sum_{i,l}\omega_l^2\hat{X}^2_{il} + \sum_{i,l,\sigma}\lambda_l\,\hat{n}_{il\sigma}\hat{X}_{il} - \sum_{i,\langle ll'\rangle,\sigma}(t_{ll'}\,\hat{c}^\dagger_{il\sigma}\hat{c}_{il'\sigma} + \text{H.c.})\,. \quad (1)$$

$\hat{c}_{il\sigma}$ ($\hat{c}^\dagger_{il\sigma}$) are annihilation (creation) operators for an electron on layer $l(=\pm1)$, site i with spin σ, and $\hat{n}_{il\sigma} = \hat{c}^\dagger_{il\sigma}\hat{c}_{il\sigma}$ is the number operator. t_l and $t_{ll'} = t_3$ denote the intra- and interlayer hopping, respectively. Phonons are represented by local (dispersionless) quantum harmonic oscillators with frequency ω_l, and on-site electron-phonon interaction on layer l is introduced via λ_l. We choose intralayer hopping $t_l = t = 1$ throughout this work to set the energy scale, and all simulations are done at half-filling $\langle\hat{n}_{il}\rangle = 1$, which can be achieved by setting the chemical potential $\mu_l = -\lambda_l^2/\omega_l^2$; phonon mass is set as $M = 1$. Each layer is an $L \times L$ site square lattice, as sketched in the inset of Fig. 1(b), with $N = 2 \times L \times L$ being the total number of sites. We focus on two cases in this work: a uniform bilayer Holstein model where $t_1 = t_{-1} = t$, $\mu_1 = \mu_{-1} = \mu$, $\omega_1 = \omega_{-1} = \omega$, and $\lambda_{+1} = \lambda_{-1} = \lambda$; and an interface between Holstein layer and "metal" layer, where only layer $l = +1$ has a nonzero electron-phonon coupling $\lambda_{+1} \neq 0$ and layer $l = -1$ has $\lambda_{-1} = 0$. We employ a recently developed Langevin QMC method [47] discussed in the next section.

We first define the local observables including the (layer-dependent) double occupancy,

$$\mathcal{D}_l \equiv \langle\hat{n}_{il\uparrow}\hat{n}_{il\downarrow}\rangle, \quad (2)$$

the near-neighbor intralayer Green's function,

$$\mathcal{G}_{\langle ij\rangle l} \equiv -\langle\hat{c}^\dagger_{il\sigma}\hat{c}_{jl\sigma} + \hat{c}^\dagger_{jl\sigma}\hat{c}_{il\sigma}\rangle, \quad (3)$$

and the near-neighbor interlayer Green's function,

$$\mathcal{G}_{\langle ll'\rangle} \equiv -\langle\hat{c}^\dagger_{il\sigma}\hat{c}_{il'\sigma} + \hat{c}^\dagger_{il'\sigma}\hat{c}_{il\sigma}\rangle. \quad (4)$$

When multiplied by their associated hopping integrals, $t\mathcal{G}_{\langle ij\rangle l}$ and $t_3\mathcal{G}_{\langle ll'\rangle}$ give the intra- and interlayer kinetic energies per site.

Two further observables, the density-density and pair-pair correlators, aid in characterizing the excitations between the planes.

$$d_{-1,1} \equiv \tfrac{1}{4}\langle\hat{n}_{i,1}\hat{n}_{i,-1} - 1\rangle,$$
$$p_{-1,1} \equiv -\tfrac{1}{4}\langle\hat{\Delta}_{i,1}\hat{\Delta}^\dagger_{i,-1} + \hat{\Delta}^\dagger_{i,1}\hat{\Delta}_{i,-1}\rangle,$$
$$\hat{\Delta}^\dagger_{il} \equiv \hat{c}^\dagger_{il\uparrow}\hat{c}^\dagger_{il\downarrow}. \quad (5)$$

$d_{-1,1}$ and $p_{-1,1}$ are the analogs of the zz and xy spin correlations which enter into the characterization of interlayer singlet formation in the Hubbard and Heisenberg bilayers (see Appendix A). Because of rotational symmetry of those models, their magnetic analogs, obtained by the transformation $\hat{c}_{il\downarrow} \to \hat{c}^\dagger_{il\downarrow}$ are identical in value. $d_{-1,1} = p_{-1,1}$ would also hold in the attractive Hubbard Hamiltonian. Here, in the Holstein model, rotational symmetry is broken and we have $d_{-1,1} \neq p_{-1,1}$. We will discuss the implications further in the sections to follow.

Characterization of the CDW formation in the thermodynamic limit can be made by the analysis of the (layer-resolved) structure factor,

$$S^{\rm CDW}_l = \frac{2}{N}\sum_{ij}(-1)^{i+j}\langle\hat{n}_{il}\hat{n}_{jl}\rangle, \quad (6)$$

with $\hat{n}_{il} = \sum_\sigma \hat{n}_{il\sigma}$. $S^{\rm CDW}_l$ samples correlations across the entire lattice, and hence is a primary tool in the determination of long-range order.

In the case of the uniform bilayer, the quantities defined in Eqs. (2)–(4) and (6) are independent of the layer index l,

and in this case we suppress this index. But for the "interface" geometry, which includes one layer with $\lambda_1 \neq 0$ and another with $\lambda_{-1} = 0$, measurements performed on the two layers are inequivalent.

The layer-resolved single-particle spectral function $A_l(\omega)$ is obtained by using the maximum entropy method to invert the integral equation relating the imaginary time-dependent Green's function $G_{i=0}(\tau)$ and $A(\omega)$:

$$G_{i=0}(\tau) = \int d\omega \frac{e^{-\tau\omega}}{1+e^{\beta\omega}} A(\omega),$$

$$G_i(\tau) = \langle \hat{c}_i(\tau)\hat{c}_0^\dagger(0)\rangle = \langle e^{\tau\mathcal{H}}\hat{c}_i(0)e^{-\tau\mathcal{H}}\hat{c}_0^\dagger(0)\rangle. \quad (7)$$

τ represents imaginary time; layer and spin indices are omitted here for simplicity. The appropriate local G is used to get $A_l(\omega)$ for each layer l in the interface geometry.

We advance our key results in Figs. 1(a) and 1(b): (i) At weak t_3 there is a phase transition at finite temperature T_c to a state with long-range charge order. In the bilayer case, T_c initially increases with t_3 as the charge order is enhanced by increased coordination number. (ii) At $T = 0$, in both the Holstein bilayer and the Holstein-metal interface, CDW order is destroyed for t_3 exceeding a quantum critical value. (iii) The phase diagram of the interface geometry exhibits an "orbitally selective CDW phase" (OSCDW) at low T and weak t_3. The specific description of how these phase diagrams are obtained is given in the corresponding section containing the main results of each model.

III. LANGEVIN SIMULATION ALGORITHM

We employ a recently developed Fourier accelerated Langevin QMC method [47]. The partition function of the Holstein Hamiltonian is written as a path integral $\mathcal{Z} = \mathrm{Tr}e^{-\beta\hat{\mathcal{H}}} = \mathrm{Tr}e^{-\Delta\tau\hat{\mathcal{H}}}e^{-\Delta\tau\hat{\mathcal{H}}}\cdots e^{-\Delta\tau\hat{\mathcal{H}}}$ where the inverse temperature $\beta = L_\tau\Delta\tau$ is discretized along the "imaginary time" axis. Complete sets of phonon eigenstates $|\{x_{i,\tau}\}\rangle$ are inserted at each time slice, allowing the action of the phonon operators to be evaluated. In so doing, we convert the quantum problem into a classical problem in one higher dimension. Since the fermion operators appear only as quadratic forms, we can trace over the associated degrees of freedom, leaving the partition function dependent only on the phonon field $\{x_{i,\tau}\}$,

$$\mathcal{Z} = \int \mathcal{D}x_{i,\tau} e^{-S_{\mathrm{ph}}}[\det M(\{x_{i,\tau}\})]^2 = \int \mathcal{D}x_{i,\tau} e^{-S}, \quad (8)$$

where the "phonon action"

$$S_{\mathrm{ph}} = \frac{\Delta\tau}{2}\left[\omega^2\sum_{i,\tau} x_{i,\tau}^2 + \sum_i\left(\frac{x_{i,\tau+1}-x_{i,\tau}}{\Delta\tau}\right)^2\right] \quad (9)$$

and

$$S = S_{\mathrm{ph}} - \ln(\det M)^2. \quad (10)$$

Here M is a sparse matrix of dimension NL_τ whose detailed form is given in Ref. [47]. The square of the determinant appears because up and down fermionic species have the same coupling to the phonons. As a consequence, there is no sign problem [48,49]. In order to sample the phonon coordinates, instead of using the usual Metropolis algorithm, we evolve $\{x_{i,\tau}\}$ using the discretized Langevin equation, whose simplest form is given by the first-order Euler discretization,

$$x_{i,\tau,t+dt} = x_{i,\tau,t} - dt\frac{\partial S}{\partial x_{i,\tau,t}} + \sqrt{2\,dt}\,\eta_{i,\tau,t}, \quad (11)$$

where t is the Langevin time, and η is a Gaussian distributed stochastic variable. In practice, in our simulations we make use of a higher-order Runge-Kutta discretization [47] which reduces the discretization error to $\mathcal{O}(dt^2)$. Throughout this work, the Langevin time step dt is chosen as 0.002, which has been shown to be sufficiently small so that the Langevin time discretization error is of the same order, or smaller than, statistical errors in typical simulations [47]. It can be demonstrated that, in the stationary limit, this Markov process generates configurations which are drawn from the exponential of the action of Eq. (10). The computational kernel is the calculation of the partial derivatives of the action via

$$\frac{\partial S}{\partial x_{i,\tau,t}} = \frac{\partial S_{\mathrm{ph}}}{\partial x_{i,\tau,t}} - 2\mathrm{Tr}\frac{\partial M}{\partial x_{i,\tau,t}}M^{-1}, \quad (12)$$

where the trace is evaluated using a stochastic estimator [47]. Comparing to the conventional determinant quantum Monte Carlo method, which is an $O(N^3L_\tau)$ approach, the Langevin method scales as $O(NL_\tau)$ (although with a larger prefactor, so that there is a crossover N at which the Langevin approach becomes the more efficient method). This enables simulations to reach considerably larger lattice sizes. In this work, we analyze systems up to $N = 800$ sites. The efficiency of the Langevin approach results from the sparsity of the matrix M and the fact that computing the action of M^{-1} on a vector can be done iteratively in a number of steps which does not grow with N [47], with appropriate preconditioning. The Langevin dynamics we employ is particularly effective in the adiabatic limit of small phonon frequencies, where the density of zeros of individual fermion determinants is negligible [50]. In what follows we fix $\omega = 0.1$, thus simulations are stable, and statistical convergence is quickly obtained over the course of Markov generation.

IV. HOLSTEIN BILAYER

We initially consider two identical layers with λ=0.2, $\omega = 0.1$ and the question of the destruction of CDW order via the formation of charge singlets at large interlayer hopping t_3 before tackling the more complex issue of selective CDW transitions.

Figure 2(a) gives the CDW structure factor S^{cdw} as a function of t_3 at low temperature for two lattice sizes. Below $t_{3,c} \approx 4.8$, S^{cdw} is large, and grows with lattice size, suggesting long-range charge order. Figure 2(b) focuses on the interlayer density-density $d_{-1,1}$ and pair-pair $p_{-1,1}$ correlations. For small t_3, only $d_{-1,1}$ is large in magnitude, indicating coherence in the charge order between the two layers. As t_3 increases, intersheet pair correlations $p_{-1,1}$ develop. $d_{-1,1}$ and $p_{-1,1}$ then become nearly degenerate at $t_{3,c}$, signaling the loss of CDW order and entry into the "charge singlet" phase. Together, Figs. 2(a) and 2(b) motivate the bilayer phase diagram of Fig. 1(a).

Although the QCP in this Holstein bilayer is closely analogous to that occurring in Hubbard and Heisenberg bilayers

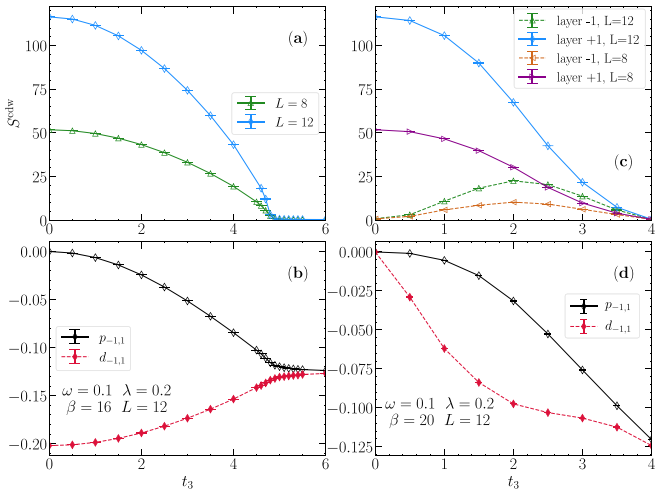

FIG. 2. (a) Charge structure factor S^{CDW} and (b) $p_{-1,1}$ and $d_{-1,1}$ as a function of interlayer hopping t_3 for the Holstein bilayer at low temperature $\beta = 16$ and $\lambda_{+1} = \lambda_{-1} = 0.2$. S^{CDW} shows significant finite size effects in the ordered phase $t_3 \lesssim 4.8$. Note that $d_{-1,1}$ vanishes at $t_3 = 0$, but jumps discontinuously to a nonzero value for infinitesimal t_3. Panels (c) and (d) are analogs of (a) and (b) for the Holstein-metal interface. The two curves in (c) correspond to layers $l = +1$ and $l = -1$, with $\lambda_{+1} = 0.2$ and $\lambda_{-1} = 0$, respectively, and temperature $\beta = 20$. In all plots the phonon frequency is set at $\omega = 0.1$.

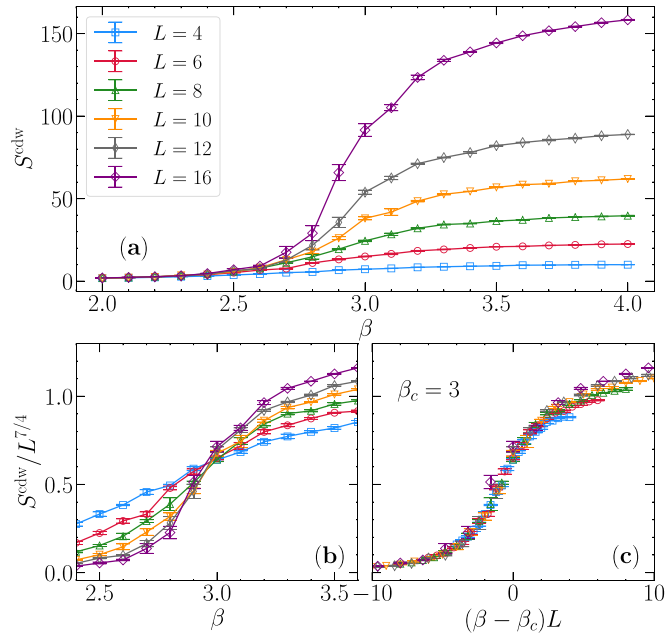

FIG. 3. (a) CDW structure factor S^{CDW} dependence on the inverse temperature β and finite size scaling of the Holstein bilayer at $t_3 = 2$. Both the crossing plot (b) and the full data collapse (c) using 2D Ising critical exponents and $\beta_c \simeq 3.0$.

as well as the periodic Anderson model, in those cases the electron-electron interaction gives rise to magnetic phases which form due to the breaking of a *continuous* spin symmetry. Thus in two-dimensional (2D) and quasi-2D geometries, no long-range order is possible at finite T. In contrast, here for the Holstein model, charge and pairing order are not degenerate, as emphasized by the data of Fig. 2(b). CDW correlations dominate at half-filling and a finite temperature phase transition can occur, terminating at a QCP as shown in Figs. 1(a) and 1(b). This distinction means that, in principle, our characterization of the unordered phase as a "charge singlet" is somewhat loose: in the usual spin singlet the x, y, z components of the spin-spin correlations on the two layers (or in the two orbitals) are equal. With that said, the equivalence of $p_{-1,1}$ and $d_{-1,1}$ in the large t_3 regime points to an emergent restoration of the symmetry (see Appendix A). It is worth noting that in the absence of t_3, e.g., in the 2D Holstein model, this restoration does not occur until the antiadiabatic limit is reached, which requires very large values of ω [51].

Figure 3 provides details of the behavior of the CDW structure factor. The top panel (a) gives raw values for S^{CDW} as a function of β at $t_3 = 2$ for different lattice sizes. At low β (high temperature), the correlation length ξ is short and S^{CDW} is independent of L. As β increases, so does ξ and when $\xi \sim L$, S^{CDW} becomes sensitive to L. This separation of the curves provides a crude estimate for β_c, which may then be determined precisely by finite size scaling (FSS).

In particular, in the vicinity of the critical temperature T_c, the CDW structure factor measured on finite lattices of linear dimension L should obey

$$S^{\mathrm{CDW}} \sim L^{\gamma/\nu} f\left(\frac{T - T_c}{T_c} L^{1/\nu}\right). \tag{13}$$

As a consequence, when plotting $S^{\mathrm{CDW}}/L^{\gamma/\nu}$ as a function of the inverse temperature β, different sizes L cross at $\beta = \beta_c$ [Fig. 3(b)]. Following the scaling form given in Eq. (13) we note that when plotted against $(\beta - \beta_c)L^{1/\nu}$ all data collapse on a single curve [see Fig. 3(c) (and later for the Holstein-metal interface in Fig. 5)]. In this analysis we have used the critical exponents of the 2D Ising universality class ($\gamma = 7/4$ and $\nu = 1$), since the CDW phase breaks a Z_2 symmetry. A discussion of the degree to which the collapse worsens, and hence the accuracy with which the exponents can be determined, is given in Appendix B.

Using such scaling procedure for various values of the interplane hybridization, allows us to extract the location of the thermal transition, as compiled in Fig. 1(a), using two values of the electron-phonon interaction. In this geometry, the critical temperature T_c initially increases as a consequence of the larger coordination number when the planes are coupled—the 2D to 3D crossover. However, at large t_3 the critical temperature decreases and ultimately vanishes at a quantum critical point.

V. HOLSTEIN-METAL INTERFACE

We next consider the "Holstein-metal interface" in which layer $l = +1$ has nonzero λ_{+1} but $\lambda_{-1} = 0$. The two layers are in contact via hybridization. Here, in addition to the question of charge singlet formation at large t_3, quenching CDW order, a different fundamental question arises: to what extent do CDW correlations in layer $l = +1$ "penetrate" into layer $l = -1$, and, conversely, is the CDW in layer $l = +1$ disrupted by contact with the metallic layer? We choose $\lambda = 0.2$ and $\omega = 0.1$ as in the previous section.

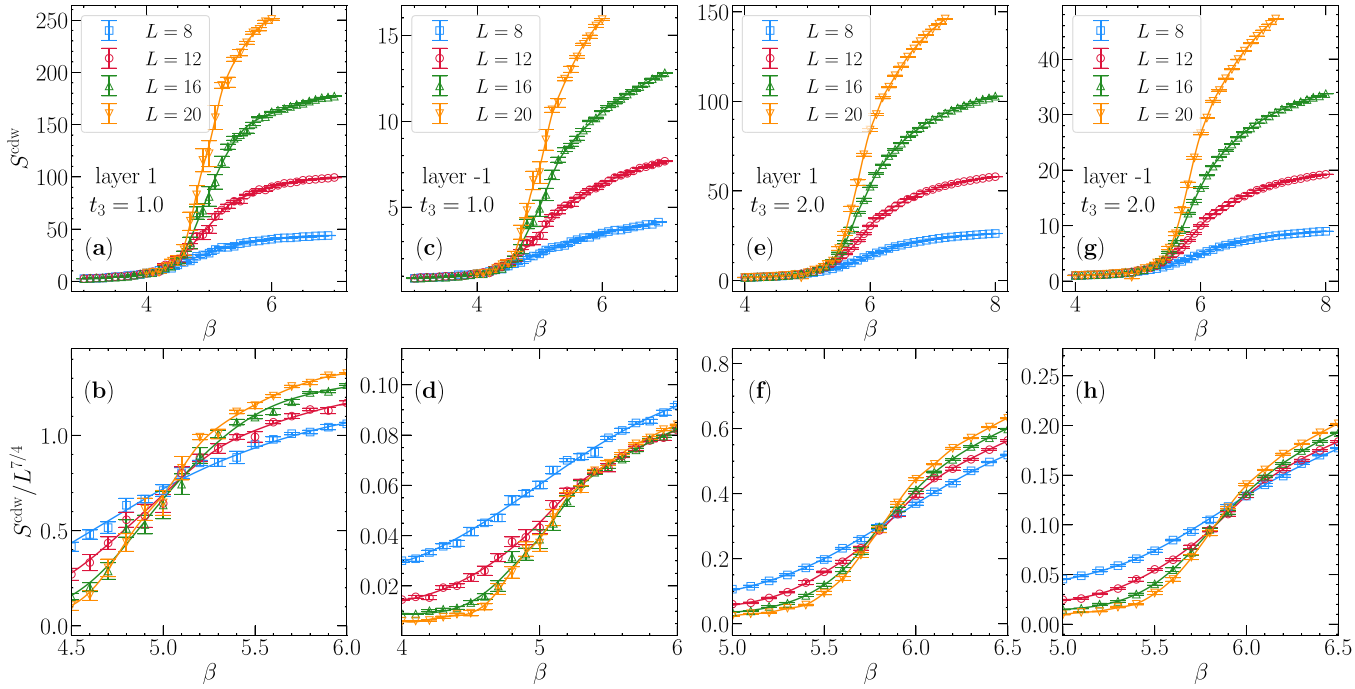

FIG. 4. (a) CDW structure factor, S^{CDW}, dependence on the inverse temperature, β, for layer $l = 1$ of the Holstein interface at $t_3 = 1$; (b) using 2D Ising critical exponents for finite size scaling (FSS). Panels (c) and (d) display the same but for the metallic layer $l = -1$. Panels (e)–(h) display the corresponding data for $t_3 = 2$. FSS in (f) and (h) show the same critical temperature for both layers at $t_3 = 2$, in contrast to $t_3 = 1$, where layer $l = +1$ (b) exhibits a clear CDW transition whereas data for layer $l = -1$ (d) does not exhibit crossing when using Ising critical exponents.

Figure 2(c) shows the CDW structure factor S^{CDW} in the two layers. S^{CDW}_{+1} decreases steadily with t_3: additional quantum fluctuations associated with contact with the metal reduce charge order. In contrast, S^{CDW}_{-1} is nonmonotonic: charge order is initially induced in the metal via contact with the Holstein layer, but ultimately large t_3 is inimical to it. The behavior of S^{CDW}_{-1} provides a first clue that order in layer $l = -1$ might occur only for intermediate t_3. Figure 2(d) gives the interlayer density-density $d_{-1,1}$ and pair-pair $p_{-1,1}$ correlations for this interface geometry. The primary difference from the original bilayer case is the gradual development of $d_{-1,1}$ with t_3. This is a consequence of the absence of CDW in the metal layer when t_3 vanishes. The interlayer hopping thus must not only couple the charge correlations, but also induce them in layer $l = -1$. Similar to the bilayer case, $d_{-1,1}$ and $p_{-1,1}$ become degenerate for large t_3. This is again a signature of entering into the charge singlet phase. We now turn to a more careful FSS study of the layer-resolved S^{CDW}_l. Our main interest is in determining how long-range order in the two layers evolves with t_3. Figure 4 displays a detailed analysis of two representative values, $t_3 = 1$ and $t_3 = 2$. The former is a case when S^{CDW}_{-1} is just beginning to develop, and the latter is when S^{CDW}_{-1} has reached its maximal induced value [see Fig. 2(c)]. There is a superficial resemblance in the unscaled data for both values of t_3, which rise as the temperature is lowered (β increases) and also increase with system size. A proper scaling

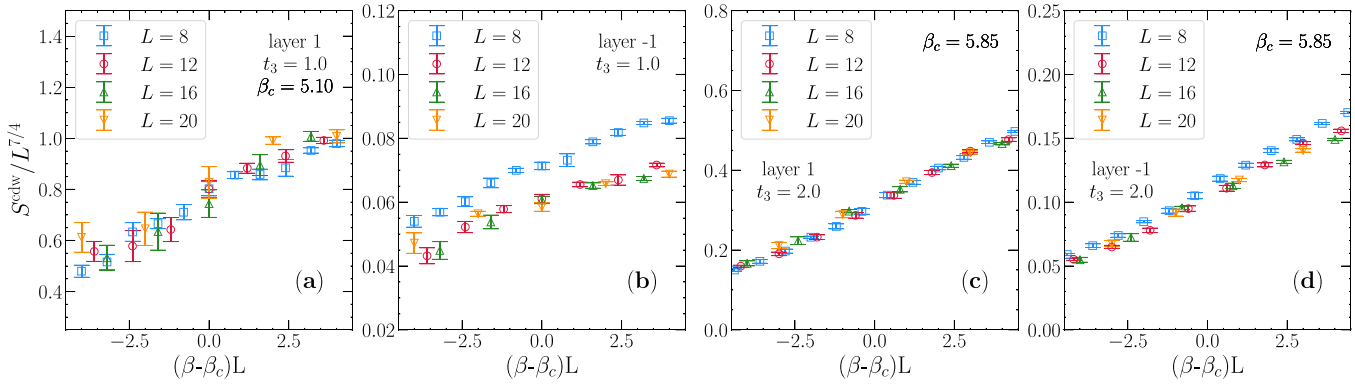

FIG. 5. Full data collapse of the scaled CDW order parameter versus scaled reduced temperature in the "Holstein interface" system. Only the Holstein layer (layer 1) shows a single universal curve for $t_3 = 1$ (a), while both collapse for $t_3 = 2t$ [panels (c) and (d)].

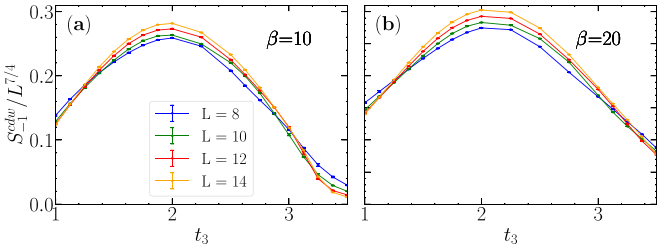

FIG. 6. Crossing plot of $S^{\mathrm{CDW}}_{-1}/L^{7/4}$ (metallic layer) versus t_3 at $\lambda = 0.2$ and $\omega = 0.1$, at low temperature (a) $\beta = 10$ and (b) $\beta = 20$, for the Holstein-metal interface. Two crossings are seen in each case: (a) $t_3 \sim 1.3$ and $t_3 \sim 3.2$ ($\beta = 20$) and (b) $t_3 \sim 1.33$ and $t_3 \sim 3.1$ ($\beta = 10$). All crossings are obtained with the critical exponents of the two-dimensional Ising model consistent with breaking the discrete Z_2 symmetry. The metallic layer, $l = -1$, is in the CDW phase only between the two values of t_3 where the curves cross.

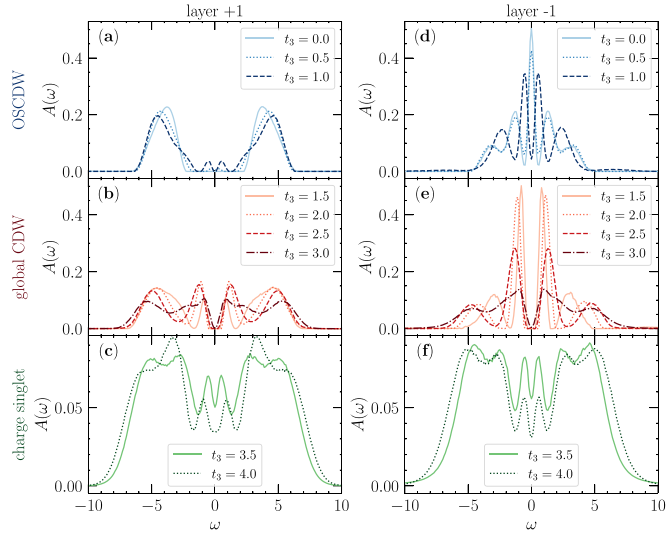

FIG. 7. Spectral function $A(\omega)$ at $\beta = 12$ for several t_3 values cutting across the Holstein-metal interface phase diagram of Fig. 1. Top: Small t_3. Middle: Intermediate t_3. Bottom: Large t_3. Left and right columns correspond to Holstein and metallic layers $l = +1$ and $l = -1$, respectively.

analysis, however, reveals a profound distinction. As seen in Figs. 4(b) and 4(f), for both values of t_3, the layer $l = +1$ with nonzero electron-phonon coupling $\lambda_{+1} = 0.2$, has a scaled structure factor $L^{-7/4}S^{\mathrm{CDW}}_{+1}$ which exhibits a sharp crossing, indicating a finite temperature transition to long-range CDW order. When $t_3 = 2$, this crossing occurs for the metallic layer with $\lambda_{-1} = 0$ as well [Fig. 4(h)]. However, when $t_3 = 1$ the data for the metallic layer do not cross for the studied system sizes [Fig. 4(d)], namely, $L = 8$–20 for both t_3 values: The $L = 12, 16$ and 20 curves converge at $\beta > 5.4$ instead of crossing. The $L = 8$ data do not scale with the other lattice sizes at all. This distinction becomes even more apparent in Fig. 5, where a simultaneous data collapse for the scaled structure factor can be made possible at the same temperature for $t_3 = 2$, while it is unattainable for $t_3 = 1$.

We conclude that for $t_3 = 2$, the interface geometry has CDW order in both layers, with long-range correlations in the metallic layer induced by proximity to the Holstein layer. For $t_3 = t$, the interface geometry exhibits *orbital-selective* CDW order—the metal remains with only short-range correlation despite its hybridization to the long-range CDW layer. This conclusion is supported by the data in Fig. 6, where sweeps of the scaled S^{CDW} with t_3 at two values $\beta = 20$, 10 show a pair of crossings. For $\beta = 20$ these occur at $t_3 \sim 1.3$ and $t_3 \sim 3.2$ and for $\beta = 10$ at $t_3 \sim 1.33$ and $t_3 \sim 3.1$. This analysis indicates that long-range CDW order exists in layer $l = -1$ only between these values of t_3. In particular, for t_3 less than the lower critical value, layer $l = -1$ is not in a CDW phase while layer $l = +1$ is. All crossings are obtained with critical exponents, of the two-dimensional Ising model, as expected since a Z_2 symmetry is being broken.

VI. SPECTRAL FUNCTIONS AND DOUBLE OCCUPANCIES

Having examined structure factors and interlayer correlators, we now turn to the spectral functions and the double occupancies, both of which provide additional insight into the ground state properties. The layer-resolved spectral functions $A_l(\omega)$, shown in Fig. 7, the many-body analog of the single-particle density of states, provide confirming evidence for the Holstein interface phase diagram of Fig. 1(b). In the top row, for small t_3, the Holstein layer $l = +1$ exhibits a CDW gap. The gap at $t_3 = 0$ is large; hybridization with the metal produces peaks closer to $\omega = 0$, but a smaller gap remains. On the other hand, the metal layer $l = -1$ has finite Fermi surface spectral weight $A_{-1}(\omega = 0) \neq 0$, thus showing the OSCDW. In the middle row, for intermediate t_3, both layers have a gap, consistent with the measurement of simultaneous long-range CDW order. Finally, in the bottom row, for large t_3, both layers have finite Fermi surface spectral weight $A_l(\omega = 0) \neq 0$ for $l = +1, -1$. The system is in the charge singlet (charge liquid) phase.

We note that although the bilayer and interface geometries have many properties in common at large t_3, their spectral functions are different. There is a gap in the bilayer case, but not for the interface. We have verified, with separate exact diagonalization calculations, that for dimers (i.e., $t_3 \gg t$) with $\lambda_{+1} = \lambda_{-1}$ one finds $A(\omega)$ is gapped, while when λ_{+1} is nonzero $\lambda_{-1} = 0$ one reproduces the behavior shown in Figs. 7(c) and 7(f).

In a perfect CDW phase, half of the sites are doubly occupied and half are empty, and $\mathcal{D} = 0.5$. In the absence of interactions, $\lambda = 0$, all four site occupation possibilities $|0\rangle$, $|\uparrow\rangle$, $|\downarrow\rangle$, and $|\uparrow\downarrow\rangle$ are equally likely and $\mathcal{D} = 0.25$. This is also the case in the charge singlet phase. Figure 8 shows $\mathcal{D}$ as a function of t_3. Panel (a) is for the bilayer, where $\mathcal{D}_{+1} = \mathcal{D}_{-1}$, and panel (b) for the interface geometry where the two are inequivalent. In both cases, $\mathcal{D}_{+1}$ is seen to evolve between the CDW and singlet limits, although it never attains the value $\mathcal{D} = 0.5$ owing to the presence of quantum fluctuations. For the interface, $\mathcal{D}_{-1}$ begins at the uncorrelated value $\mathcal{D}_{-1} = 0.25$ at $t_3 = 0$ since $\lambda_{-1} = 0$. The double occupancy evolution is quite similar to that of the structure factor, Figs. 2(a) and 2(c). However, since $\mathcal{D}$ is a local observable, it exhibits less sharp features than S^{CDW} in the vicinity of the QCP and thus only provides qualitative evidence for a crossover between those two phases. Besides that, a simple

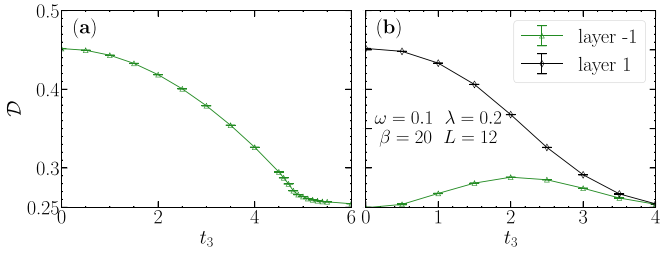

FIG. 8. Double occupancy $\mathcal{D}$ shown as a function of interlayer hopping t_3 at low temperature $\beta = 20$. $\mathcal{D}$ is a local observable, and its value is the same for $L = 8$ and $L = 12$ to within the symbol size; we show the latter. (a) Holstein bilayer. (b) Holstein-metal interface. In (a) the two layers are equivalent and a single curve is shown. In (b) the green curve shows data on layer $l = -1$, whereas the gray curve represents layer $l = +1$.

model which exhibits a layer-dependent trivial CDW formation with only electronic degrees of freedom, a bilayer ionic model, already displays this characteristic nonmonotonicity with growing hybridization (see Appendix C).

VII. DISCUSSION AND CONCLUSIONS

We have generalized our existing understanding of the effect of interlayer/interorbital hybridization t_3 on *magnetic* order driven by an on-site *electron-electron repulsion* in the Hubbard model to *charge* order originating in *electron-phonon interactions* in the Holstein model. The two scenarios, although qualitatively related, are quite distinct in detail owing to the lower symmetry of the CDW order parameter relative to the magnetic case. Despite this difference, and its consequences such as the appearance of charge order at finite temperature, the basic feature of the destruction of long-range order in the limit of large hybridization is shown still to occur. Indeed, one remarkable conclusion of our work is that t_3 seems to restore the degeneracy of pairing and charge correlations at the QCP.

Our most interesting observation is that the coexistence of CDW order on a layer with nonzero electron-phonon coupling λ with a metallic phase on the $\lambda = 0$ layer, which is trivially true at $t_3 = 0$, likely extends out to finite t_3. This conclusion is based on the inability to scale the charge correlations in the $\lambda = 0$ layer unless $t_3 \gtrsim 1.4$ (for $\lambda_{+1} = 0.2$).

The possibility that charge order takes place selectively parallels the known occurrence of distinct Mott transitions in multiorbital Hubbard models in the coexistence of metallic and insulating behavior. However, the connection is not exact, since in principle a Mott transition might occur in the absence of spontaneous symmetry breaking, whereas the insulating CDW phase here breaks Z_2 symmetry. With that said, the Mott transition in its most common incarnation, the square lattice Hubbard model, *is* always accompanied by long-range antiferromagnetic order. Thus our work does provide a close analog of the case of orbital-selective transitions in bands with differing electron-electron interaction strengths.

ACKNOWLEDGMENTS

The work of Y.X.Z., C.H.F., and R.T.S. was supported by Grant No. DE-SC0014671 funded by the U.S. Department of Energy (DOE), Office of Science, Basic Energy Sciences (BES). R.M. acknowledges support from the National Natural Science Foundation of China (NSFC) Grants No. U1930402, No. 12050410263, No. 12111530010, No. 11974039, and No. 12222401.

Y.X.Z., C.H.F., and R.T.S. were responsible for the concept of the project and conducted the quantum simulations, primary data analysis, and manuscript composition. R.M. and G.B. were responsible for additional analysis of data and manuscript composition.

APPENDIX A: CONNECTION TO MAGNETIC LANGUAGE

In the repulsive 2D Hubbard model the dominant physics at half-filling on a bipartite lattice is antiferromagnetic order, characterized by the operators

$$\begin{aligned}
\hat{S}^j_x &= \tfrac{1}{2}(\hat{S}^j_+ + \hat{S}^j_-) = \tfrac{1}{2}(\hat{c}^\dagger_{j\uparrow}\hat{c}_{j\downarrow} + \hat{c}^\dagger_{j\downarrow}\hat{c}_{j\uparrow}),\\
\hat{S}^j_y &= \tfrac{1}{2i}(\hat{S}^j_+ - \hat{S}^j_-) = \tfrac{1}{2i}(\hat{c}^\dagger_{j\uparrow}\hat{c}_{j\downarrow} - \hat{c}^\dagger_{j\downarrow}\hat{c}_{j\uparrow}),\\
\hat{S}^j_z &= \tfrac{1}{2}(\hat{n}_{j\uparrow} - \hat{n}_{j\downarrow}) = \tfrac{1}{2}(\hat{c}^\dagger_{j\uparrow}\hat{c}_{j\uparrow} - \hat{c}^\dagger_{j\downarrow}\hat{c}_{j\downarrow}).
\end{aligned} \tag{A1}$$

From these relations, and as a consequence of the spin SU(2) symmetry of the Hubbard model,

$$\begin{aligned}
&\langle \hat{S}^j_+\hat{S}^i_- + \hat{S}^j_-\hat{S}^i_+\rangle = 4\langle \hat{S}^j_z\hat{S}^i_z\rangle, \quad \langle \hat{c}^\dagger_{j\uparrow}\hat{c}_{j\downarrow}\hat{c}^\dagger_{i\downarrow}\hat{c}_{i\uparrow} + \hat{c}^\dagger_{j\downarrow}\hat{c}_{j\uparrow}\hat{c}^\dagger_{i\uparrow}\hat{c}_{i\downarrow}\rangle\\
&= \langle (\hat{c}^\dagger_{j\uparrow}\hat{c}_{j\uparrow} - \hat{c}^\dagger_{j\downarrow}\hat{c}_{j\downarrow})(\hat{c}^\dagger_{i\uparrow}\hat{c}_{i\uparrow} - \hat{c}^\dagger_{i\downarrow}\hat{c}_{i\downarrow})\rangle.
\end{aligned} \tag{A2}$$

If we perform a particle-hole transformation to the down spin fermions,

$$\begin{aligned}
\hat{c}^\dagger_{j\downarrow} &\to (-1)^j\hat{c}_{j\downarrow},\\
\hat{n}_{j\downarrow} &\to (1 - \hat{n}_{j\downarrow}),\\
\hat{S}^j_+ = \hat{c}^\dagger_{j\uparrow}\hat{c}_{j\downarrow} &\to (-1)^j\hat{c}^\dagger_{j\uparrow}\hat{c}^\dagger_{j\downarrow} \equiv (-1)^j\hat{\Delta}^\dagger_j,\\
\hat{S}^j_z = \tfrac{1}{2}(\hat{n}_{j\uparrow} - \hat{n}_{j\downarrow}) &\to \tfrac{1}{2}(\hat{n}_{j\uparrow} + \hat{n}_{j\downarrow}) \equiv \hat{n}_j
\end{aligned} \tag{A3}$$

we conclude that

$$-\langle \hat{\Delta}^\dagger_j\hat{\Delta}_i + \hat{\Delta}_i\hat{\Delta}^\dagger_j\rangle = \langle (\hat{n}_j - 1)(\hat{n}_i - 1)\rangle \tag{A4}$$

assuming that sites i and j are on opposite sublattices.

If, finally, assuming we are at half-filling, so that $\langle \hat{n}_j\rangle = 1$,

$$-\langle \hat{\Delta}^\dagger_j\hat{\Delta}_i + \hat{\Delta}_i\hat{\Delta}^\dagger_j\rangle = \langle \hat{n}_j\hat{n}_i - 1\rangle. \tag{A5}$$

This shows that the two correlation functions of Eq. (5) are equal: $p_{1,-1} = d_{1,-1}$. The merging of the two curves of Figs. 2(c) and 2(d) at a common value reflects a restoration of an SU(2) symmetry of the Hubbard model. It is interesting that this occurs even though the correlators are not in the singlet limit of $-1/4$ (due to the fact that we are not in Holstein analog of the large U limit).

APPENDIX B: EXTRACTING THE CRITICAL EXPONENTS

We argue that owing to the symmetry of the order parameter of the CDW phase, we make use of the critical exponents pertaining to the 2D Ising universality class in order to simplify the FSS of the CDW structure factor S^{CDW}. Here, we justify this choice by quantitatively extracting the best set of exponents ν and γ that scales the curves according to the

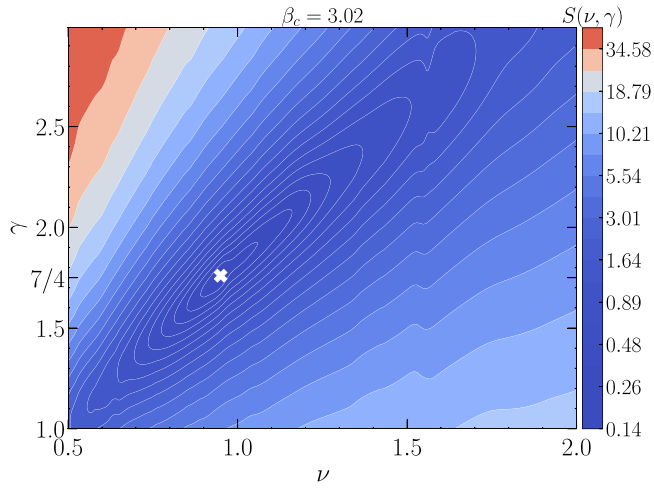

FIG. 9. Contour plot of the sum of squared residuals of the least-squares fit $S(\nu,\gamma)$ of the scaled data for the CDW structure factor S^{CDW} of the Holstein bilayer at $t_3 = 2$ (see Fig. 3 for the original data). A 16th-order polynomial is used to fit the data set, and the critical inverse temperature used is $\beta_c = 3.02$. The white marker denotes the minimum $S(\nu,\gamma)$ which occurs at $\nu = 0.95$ and $\gamma = 1.7$, agreeing with the 2D Ising exponents.

functional form in Eq. (13). We start by using the scaled data in a large range of critical exponents; subsequently, for each pair of (ν,γ), we proceed with a high-order polynomial fitting of the scaled data, storing the residual $S(\nu,\gamma)$ of the fitting procedure. The set of exponents that minimizes $S(\nu,\gamma)$ is taken as those that characterize the transition. The rationale is that if the dataset is well collapsed for a given (ν,γ),

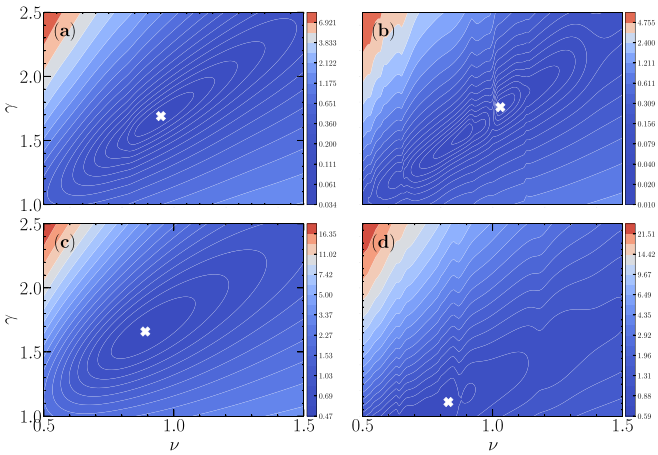

FIG. 10. Contour plot of the sum of squared residuals of the least-squares fit $S(\nu,\gamma)$ of the scaled data for the CDW structure factor S^{CDW} of the Holstein interface; top row at $t_3 = 2$; bottom row at $t_3 = 1$; left column: layer $l = +1$; right column: layer $l = -1$. (See Fig. 4 for the original data.) A 16th order polynomial is used to fit the data set, and the critical inverse temperatures used are listed in Fig. 5. The white marker denotes the minimum $S(\nu,\gamma)$ in the displayed range of ν and γ. In panels (a), (b), and (c), minimum residuals are at $(\nu = 0.95, \gamma = 1.69)$, $(\nu = 1.03, \gamma = 1.76)$, and $(\nu = 0.89, \gamma = 1.66)$, respectively, whereas in panel (d) the minimum occurs at $\nu = 0.83$, $\gamma = 1.11$. Unlike panels (a), (b), and (c), the $t_3 = 1$ metallic layer of panel (d) does not fit the known Ising exponents, suggesting the absence of order in this case.

a high-order polynomial fit (with the number of degrees of freedom much smaller than the number of data points) will turn out to have a fairly small error.

Using this procedure, we show in Fig. 9 the contour plot $S(\nu,\gamma)$ for the data corresponding to the Holstein bilayer at $t_3 = 2$. The minimum residual is indicated by the white marker. By observing its variation with slightly different critical inverse temperature β_c, and different polynomial orders used in the fits, we estimate $\nu = 0.95 \pm 0.07$ and $\gamma = 1.7 \pm 0.1$, in agreement with the 2D Ising exponents $\nu_{\text{2D Ising}} = 1$ and $\gamma_{\text{2D Ising}} = 7/4$. The formation of the CDW phase establishes long-range order by breaking the Z_2 sublattice symmetry, which is the 2D Ising universality class.

We apply the same analysis to the interface model, as shown in Fig. 10 (see Figs. 4 and 5 for original data). Both layers at $t_3 = 2$ as well as layer $l = +1$ at $t_3 = 1$ minimize the residual close to the 2D Ising critical exponents. However, in the case of layer $l = -1$ at $t_3 = 1$, the minimum residue is located at $\nu = 0.83$, $\gamma = 1.11$ which is far from the 2D Ising exponents. This supports our conclusion that there is no phase transition at $t_3 = 1$ in layer $l = -1$ since a transition into a phase with long-range CDW order necessarily breaks the Z_2 symmetry and must be in the Ising universality class.

APPENDIX C: INDUCED CDW IN IONIC HUBBARD MODEL

We can get additional insight into the Holstein interface by considering the following noninteracting, spinless, tight-binding Hamiltonian:

$$\hat{\mathcal{H}}_{\text{BI-M}} = -t \sum_{\langle ij\rangle,l} (\hat{c}^{\dagger}_{i,l}\hat{c}_{j,l} + \text{H.c.}) + \delta \sum_i (-1)^i \hat{n}_{i,1} - t_3 \sum_j (\hat{c}^{\dagger}_{j,1}\hat{c}_{j,-1} + \text{H.c.}). \tag{C1}$$

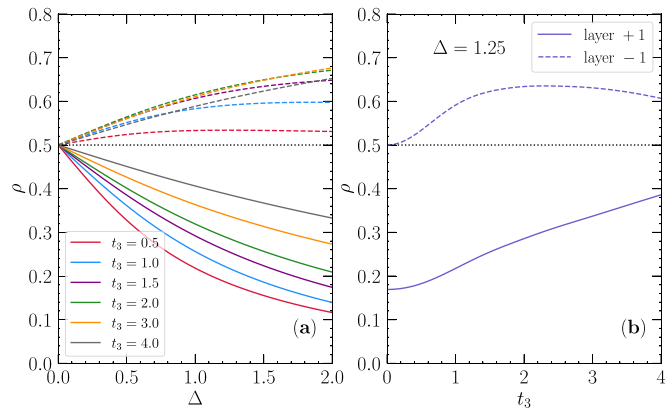

FIG. 11. Solution of the tight-binding Hamiltonian, Eq. (C1). (a) Solid curves: occupations ρ on the $+\delta$ sites of the insulating band as functions of the magnitude of the staggered potential δ; dashed curves: occupations on the partner sites in the metallic band to which those $+\delta$ sites are hybridized by t_3. (b) Solid curve: occupations on the $+\delta$ sites of the insulating band as a function of interlayer hybridization t_3; dashed curves: occupations on the partner sites in the metallic band to which those $+\delta$ sites are hybridized by t_3. The staggered potential in this case is $\delta = 1.25$. In both panels the linear lattice size and the inverse temperature are $L = 12$ and $\beta = 4$, respectively.

Equation (C1) describes two bands, labeled by $l = \pm 1$, each with hopping t on a 2D square lattice, which are hybridized with each other by t_3. Band $l = -1$ is metallic. At $t_3 = 0$ it has the usual 2D dispersion relation $\epsilon(k) = -2t\,(\cos k_x + \cos k_y)$. Band $l = +1$ is made insulating by the staggered potential δ, so that at $t_3 = 0$ its dispersion relation has two branches, $E_\pm(k) = \pm\sqrt{\epsilon(k)^2 + \delta^2}$. Both bands of Eq. (C1) are half-filled (the chemical potential $\mu = 0$).

In addition to inducing a band gap 2δ in layer $l = +1$, the staggered potential also creates a CDW phase, with low occupancy $+\delta$ and high occupancy $-\delta$ sites. Here, the CDW order is trivial, in the sense of being induced by an external field, as opposed to arising spontaneously in a symmetric Hamiltonian like the Holstein model. Nevertheless we can still examine how this "artificial" CDW in layer $l = +1$ affects the site occupations in the metallic band $l = -1$.

Figure 11(a) gives the occupations on the $+\delta$ sites of band $l = +1$ as functions of δ for different t_3. As δ grows, the occupation of the high-energy sites in layer $l = +1$, which are directly coupled to the staggered field, get increasingly small (solid curves). In turn, the occupations of the partner sites on layer $l = -1$ which are *not* coupled to δ are also shifted from $\rho = \frac{1}{2}$. These occupations increase in order to take advantage of the decrease in the Pauli blocking. What is interesting in the context of the simulations of the Holstein bilayers in the main part of this paper is that, while the layer $l = +1$ occupations steadily return to half-filling with increasing t_3, the evolution of the layer $l = -1$ occupations is instead *nonmonotonic*. The deviations of the occupations from half-filling first grow with t_3, but then shrink.

This nonmonotonicity is seen more clearly in Fig. 11(b) which plots similar occupations as a function of t_3 for a fixed δ. The maximum at intermediate $t_3 \sim 2.28$ is reminiscent of the behavior of Fig. 2(c), which similarly shows a maximum in the induced CDW order at intermediate t_3 in the metallic layer of the Holstein interface model. Indeed, the agreement between the values of t_3 at which the induced order is maximal is remarkably *quantitative*. To within error bars, the positions of the maxima are the same, although the falloff at large t_3 is more gradual in the BI-metal interface case.

[1] J. G. Bednorz and K. A. Müller, Perovskite-type oxides—The new approach to high-T_c superconductivity, Rev. Mod. Phys. **60**, 585 (1988).

[2] M. Kastner, R. Birgeneau, G. Shirane, and Y. Endoh, Magnetic, transport, and optical properties of monolayer copper oxides, Rev. Mod. Phys. **70**, 897 (1998).

[3] T. Timusk and B. Statt, The pseudogap in high-temperature superconductors: An experimental survey, Rep. Prog. Phys. **62**, 61 (1999).

[4] P. A. Lee, N. Nagaosa, and X.-G. Wen, Doping a Mott insulator: Physics of high-temperature superconductivity, Rev. Mod. Phys. **78**, 17 (2006).

[5] M. Vojta, Lattice symmetry breaking in cuprate superconductors: Stripes, nematics, and superconductivity, Adv. Phys. **58**, 699 (2009).

[6] J. M. B. Lopes dos Santos, N. M. R. Peres, and A. H. Castro Neto, Graphene Bilayer with a Twist: Electronic Structure, Phys. Rev. Lett. **99**, 256802 (2007).

[7] R. Bistritzer and A. H. MacDonald, Transport between twisted graphene layers, Phys. Rev. B **81**, 245412 (2010).

[8] G. T. de Laissardiére, D. Mayou, and L. Magaud, Localization of Dirac electrons in rotated graphene bilayers, Nano Lett. **10**, 804 (2010).

[9] J. Xue, J. Sanchez-Yamagishi, D. Bulmash, P. Jacquod, A. Deshpande, K. Watanabe, T. Taniguchi, P. Jarillo-Herrero, and B. J. LeRoy, Scanning tunnelling microscopy and spectroscopy of ultra-flat graphene on hexagonal boron nitride, Nat. Mater. **10**, 282 (2011).

[10] T. C. Lang, Z. Y. Meng, M. M. Scherer, S. Uebelacker, F. F. Assaad, A. Muramatsu, C. Honerkamp, and S. Wessel, Antiferromagnetism in the Hubbard Model on the Bernal-Stacked Honeycomb Bilayer, Phys. Rev. Lett. **109**, 126402 (2012).

[11] E. McCann and M. Koshino, The electronic properties of bilayer graphene, Rep. Prog. Phys. **76**, 056503 (2013).

[12] A. W. Sandvik and D. J. Scalapino, Order-Disorder Transition in a Two-Layer Quantum Antiferromagnet, Phys. Rev. Lett. **72**, 2777 (1994).

[13] R. T. Scalettar, J. W. Cannon, D. J. Scalapino, and R. L. Sugar, Magnetic and pairing correlations in coupled Hubbard planes, Phys. Rev. B **50**, 13419 (1994).

[14] M. Vekic, J. W. Cannon, D. J. Scalapino, R. T. Scalettar, and R. L. Sugar, Competition between Antiferromagnetic Order and Spin-Liquid Behavior in the Two-Dimensional Periodic Anderson Model at Half Filling, Phys. Rev. Lett. **74**, 2367 (1995).

[15] L. Wang, K. S. D. Beach, and A. W. Sandvik, High-precision finite-size scaling analysis of the quantum-critical point of $S = 1/2$ Heisenberg antiferromagnetic bilayers, Phys. Rev. B **73**, 014431 (2006).

[16] M. Golor, T. Reckling, L. Classen, M. M. Scherer, and S. Wessel, Ground-state phase diagram of the half-filled bilayer Hubbard model, Phys. Rev. B **90**, 195131 (2014).

[17] S. Doniach, The Kondo lattice and weak antiferromagnetism, Physica B+C **91**, 231 (1977).

[18] D. Hess, P. Riseborough, and J. Smith, in *Encyclopedia of Applied Physics*, edited by G. Trigg (VCH, New York, 1993), Vol. 7, p. 435.

[19] N. Grewe and F. Steglich, in *Handbook of Physics and Chemistry of Rare Earths*, edited by J. K. A. Gschneidner and L. L. Eyring (Elsevier, Amsterdam, 1991), Vol. 14, p. 343.

[20] A. Liebsch, Single Mott transition in the multiorbital Hubbard model, Phys. Rev. B **70**, 165103 (2004).

[21] C. Knecht, N. Blümer, and P. G. J. van Dongen, Orbital-selective Mott transitions in the anisotropic two-band Hubbard model at finite temperatures, Phys. Rev. B **72**, 081103(R) (2005).

[22] K. Bouadim, G. G. Batrouni, and R. T. Scalettar, Determinant Quantum Monte Carlo Study of the Orbitally Selective Mott Transition, Phys. Rev. Lett. **102**, 226402 (2009).

[23] A. Koga, N. Kawakami, T. M. Rice, and M. Sigrist, Orbital-Selective Mott Transitions in the Degenerate Hubbard Model, Phys. Rev. Lett. **92**, 216402 (2004).

[24] L. De Leo, M. Civelli, and G. Kotliar, $T = 0$ Heavy-Fermion Quantum Critical Point as an Orbital-Selective Mott Transition, Phys. Rev. Lett. **101**, 256404 (2008).

[25] L. de' Medici, S. R. Hassan, M. Capone, and X. Dai, Orbital-Selective Mott Transition Out of Band Degeneracy Lifting, Phys. Rev. Lett. **102**, 126401 (2009).
[26] Z.-Y. Song, H. Lee, and Y.-Z. Zhang, Possible origin of orbital selective Mott transitions in iron-based superconductors and $Ca_{2-x}Sr_xRuO_4$, New J. Phys. **17**, 033034 (2015).
[27] Z.-Y. Song, X.-C. Jiang, H.-Q. Lin, and Y.-Z. Zhang, Distinct nature of orbital-selective Mott phases dominated by low-energy local spin fluctuations, Phys. Rev. B **96**, 235119 (2017).
[28] J. Herbrych, J. Heverhagen, N. D. Patel, G. Alvarez, M. Daghofer, A. Moreo, and E. Dagotto, Novel Magnetic Block States in Low-Dimensional Iron-Based Superconductors, Phys. Rev. Lett. **123**, 027203 (2019).
[29] J. Herbrych, G. Alvarez, A. Moreo, and E. Dagotto, Block orbital-selective Mott insulators: A spin excitation analysis, Phys. Rev. B **102**, 115134 (2020).
[30] B. Pandey, L.-F. Lin, R. Soni, N. Kaushal, J. Herbrych, G. Alvarez, and E. Dagotto, Prediction of exotic magnetic states in the alkali-metal quasi-one-dimensional iron selenide compound Na_2FeSe_2, Phys. Rev. B **102**, 035149 (2020).
[31] M. Środa, E. Dagotto, and J. Herbrych, Quantum magnetism of iron-based ladders: Blocks, spirals, and spin flux, Phys. Rev. B **104**, 045128 (2021).
[32] T. Holstein, Studies of polaron motion: Part I. The molecular-crystal model, Ann. Phys. (NY) **8**, 325 (1959).
[33] R. T. Scalettar, N. E. Bickers, and D. J. Scalapino, Competition of pairing and Peierls–charge-density-wave correlations in a two-dimensional electron-phonon model, Phys. Rev. B **40**, 197 (1989).
[34] F. Marsiglio, Pairing and charge-density-wave correlations in the Holstein model at half-filling, Phys. Rev. B **42**, 2416 (1990).
[35] M. Weber and M. Hohenadler, Two-dimensional Holstein-Hubbard model: Critical temperature, Ising universality, and bipolaron liquid, Phys. Rev. B **98**, 085405 (2018).
[36] N. C. Costa, T. Blommel, W.-T. Chiu, G. Batrouni, and R. T. Scalettar, Phonon Dispersion and the Competition between Pairing and Charge Order, Phys. Rev. Lett. **120**, 187003 (2018).
[37] M. Hohenadler and G. G. Batrouni, Dominant charge density wave correlations in the Holstein model on the half-filled square lattice, Phys. Rev. B **100**, 165114 (2019).
[38] Z.-X. Li, M. L. Cohen, and D.-H. Lee, Enhancement of superconductivity by frustrating the charge order, Phys. Rev. B **100**, 245105 (2019).
[39] Y.-X. Zhang, W.-T. Chiu, N. C. Costa, G. G. Batrouni, and R. T. Scalettar, Charge Order in the Holstein Model on a Honeycomb Lattice, Phys. Rev. Lett. **122**, 077602 (2019).
[40] C. Chen, X. Y. Xu, Z. Y. Meng, and M. Hohenadler, Charge-Density-Wave Transitions of Dirac Fermions Coupled to Phonons, Phys. Rev. Lett. **122**, 077601 (2019).
[41] B. Xiao, N. C. Costa, E. Khatami, G. G. Batrouni, and R. T. Scalettar, Charge density wave and superconductivity in the disordered Holstein model, Phys. Rev. B **103**, L060501 (2021).
[42] B. Cohen-Stead, N. C. Costa, E. Khatami, and R. T. Scalettar, Effect of strain on charge density wave order in the Holstein model, Phys. Rev. B **100**, 045125 (2019).
[43] Y.-X. Zhang, H.-M. Guo, and R. T. Scalettar, Charge density wave order on a π-flux square lattice, Phys. Rev. B **101**, 205139 (2020).
[44] O. Bradley, G. G. Batrouni, and R. T. Scalettar, Superconductivity and charge density wave order in the two-dimensional Holstein model, Phys. Rev. B **103**, 235104 (2021).
[45] Studies of attractive Hubbard models, the antiadiabatic limit of the Holstein model considered here, within the dynamical cluster approximation are in progress. Philip Dee, Steven Johnston, and Thomas Maier(private communication), work in progress.
[46] C. Feng and R. T. Scalettar, Interplay of flat electronic bands with Holstein phonons, Phys. Rev. B **102**, 235152 (2020).
[47] G. G. Batrouni and R. T. Scalettar, Langevin simulations of a long-range electron-phonon model, Phys. Rev. B **99**, 035114 (2019).
[48] E. Y. Loh, J. E. Gubernatis, R. T. Scalettar, S. R. White, D. J. Scalapino, and R. L. Sugar, Sign problem in the numerical simulation of many-electron systems, Phys. Rev. B **41**, 9301 (1990).
[49] R. Mondaini, S. Tarat, and R. T. Scalettar, Quantum critical points and the sign problem, Science **375**, 418 (2022).
[50] A. Götz, S. Beyl, M. Hohenadler, and F. F. Assaad, Valence-bond solid to antiferromagnet transition in the two-dimensional Su-Schrieffer-Heeger model by Langevin dynamics, Phys. Rev. B **105**, 085151 (2022).
[51] C. Feng, H. Guo, and R. T. Scalettar, Charge density waves on a half-filled decorated honeycomb lattice, Phys. Rev. B **101**, 205103 (2020).

Correction: Specific support information has been inserted. The omission of a list of author contributions has been fixed.